

Modeling multi-jet mode electrostatic atomization using boundary element methods

S.S. Yoon^{a,*}, S.D. Heister^a, J.T. Epperson^b, P.E. Sojka^b

^a*School of Aeronautics and Astronautics, Purdue University, West Lafayette, IN 47906, USA*

^b*School of Mechanical Engineering, Purdue University, West Lafayette, IN 47906, USA*

Received 19 October 1999; received in revised form 15 June 2000; accepted 25 September 2000

Abstract

A two-dimensional, nonlinear model has been developed to assess the dynamics of charged liquid columns. The model, which is based on the boundary element method (BEM), has been used to investigate oscillations and instabilities of single and multi-column configurations. For the single-column configuration, oscillation frequencies have been determined for a range of charge and initial distortion levels. In addition, simulations of unstable jets have been conducted; these results show a “spiked” behavior at the pinching event. An energy-based analysis has been used to determine maximum voltages for stable configurations with a given number of ligaments. These results are compared against experimental data. © 2001 Elsevier Science B.V. All rights reserved.

Keywords: Electro spray; Electrostatic atomization; Boundary element method; Electrified liquid jet

1. Introduction

In many practical applications, there are significant advantages to the use of electrostatic atomization techniques. Today, this scheme is utilized in numerous fields as diverse as agricultural and automotive sprays, targeted drug delivery systems and ink-jet printers. Electrostatics are employed to provide precise control of liquid jets emanating from a circular orifice. For this reason, both statics and dynamics of electrified jets have received much attention in the research community.

* Corresponding author. Tel.: + 1-317-494-7864.

E-mail address: yoons@ecn.purdue.edu (S.S. Yoon).

The most basic dynamic behavior of electrified columns was first considered in the classic linear analyses of Lord Rayleigh [1]. Rayleigh [2] also considered the linear stability of a liquid jet subjected to axial perturbations of varying wavelengths. Numerous investigators have expanded upon these pioneering works. For example, additional linear analyses [3–6] and recent nonlinear treatments [7] have advanced liquid-jet modeling capabilities; numerous experiments have accompanied these works.

There are very few analyses of charged liquid columns, probably due to the fact that axial perturbations (as treated in the liquid-jet analyses) are of greater importance in most electrostatic atomizers. Our motivation for examining this geometry stems from recent work on multi-jet mode atomization; an atomization regime in which multiple ligaments are established in a stable configuration at the tip of a conventional orifice (see Fig. 1). Refs. [8,9] summarize recent experimental work focused on multi-jet mode operation. Multi-jet mode behavior has also been observed in the operation of colloid rocket thrusters [10], but in this application the multi-jet mode was not desirable. Cloupeau and Prunet-Foch also discuss the multi-jet regime in connection with other electrostatic operating regimes [11]. Some cone jet literature is pertinent in that it addresses the transition to multi-jet operation [12–14], but there are few studies which have focused primarily on this regime due in part to the fact that a stable behavior has not typically been noted in many instances.

In recent studies [8,9] stable behavior has been achieved for a range of flow rates and fluid resistivities; a multi-jet structure can be observed in which a number of ligaments/jets appear anchored at regular intervals about the circumference of the orifice exit. These experiments have shown that nearly mono-disperse sprays with very small-diameter drops (less than $10\mu\text{m}$) can be formed using multi-jet mode

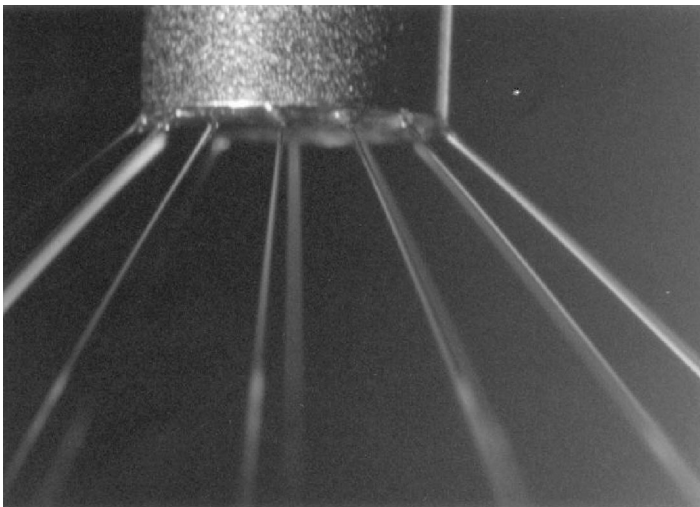


Fig. 1. Multi-jet experimental image by Epperson and Sojka [8].

operation. Due to electrostatic repulsion, the ligaments diverge at small angles from the centerline of the orifice to provide a highly structured and coherent “spray”. The interaction of the fluid columns under the radial electrostatic repulsion motivates the liquid-column studies presented herein.

Recently, a number of boundary element method (BEM) simulations have been successfully applied to free surface problems. These techniques are ideally suited to electrostatic problems in which the fluid can be assumed to be a perfect conductor. In this special case, all the charge resides on the boundary and the electrostatic potential is governed by the same differential equation as the fluid (Laplace’s equation). Models which had been developed to handle two-fluid-free surface flows [15–17] can be readily modified to incorporate electrostatic effects. The following sections provide a description of the model, followed by liquid-column simulation, and analyses of the stability of multi-jet configurations.

2. Modeling description

Since most of the details of the model have been previously discussed in the open literature (see Refs. [7,17]) we will provide just a brief description here. If we presume the fluid is inviscid, incompressible, and a perfect conductor, then both the fluid dynamics and the electrostatics are governed by Laplace’s equation. Furthermore, we assume the jets have sufficiently low speed that dynamic pressure variations induced from interaction with the gas phase are negligible. We choose the column radius (a'), applied voltage (V'_0), surface tension (σ'), and liquid density (ρ') as dimensions. Here (and throughout), primes denote dimensional quantities and unprimed variables are assumed to be dimensionless.

Under this nondimensionalization, the parameter

$$\Gamma_e = \frac{\epsilon'_0 V_0'^2}{\sigma' a'} \quad (1)$$

governs the physics of the flowfield. Here, ϵ'_0 is the permittivity of free space, and Γ_e represents the ratio of electrostatic-to-capillary pressures generated at the surface of the undisturbed column. If the charging level (Γ_e) is large enough, the electrostatic forces can cause breakup of the column.

The integral representation for the fluid velocity potential, ϕ , which is governed by Laplace’s equation, may be written as

$$\alpha\phi(\mathbf{r}_i) + \int_S \left[\phi \frac{\partial G}{\partial n} - qG \right] dS = 0, \quad (2)$$

where $\phi(\mathbf{r}_i)$ is the value of the potential at a point \mathbf{r}_i , S denotes the boundary of the domain, and G is the free-space Green’s function corresponding to Laplace’s equation. An analogous form of Eq. (2) can also be derived for the electrostatic potential, ϕ_e . For a well-posed problem, either ϕ or $q = \partial\phi/\partial n$ must be specified at each point on the boundary. Here n is the outward normal to the boundary so that q represents the

velocity normal to the boundary. The quantity α in Eq. (2) results from singularities introduced as the integration passes over the boundary point, \mathbf{r}_i .

In the case of a two-dimensional (2-D) flow (letting x and y represent the coordinates), the free-space Green's function may be written as

$$G = \frac{1}{2\pi} \ln |\mathbf{r} - \mathbf{r}_i| = \frac{1}{4\pi} \ln [(x - x_i)^2 + (y - y_i)^2]. \quad (3)$$

Both G and q are assumed to vary linearly along a given element. In this case, integration of Eq. (2) across a segment can be carried out analytically [17].

The surface is moved in a Lagrangian fashion from basic kinematics considerations:

$$\frac{Dx}{Dt} = \frac{\partial \phi}{\partial x}, \quad \frac{Dy}{Dt} = \frac{\partial \phi}{\partial y}, \quad (4)$$

where the notation $D(\)/Dt$ implies a Lagrangian derivative for points on the surface moving with the local liquid velocity and $\partial \phi / \partial x$ and $\partial \phi / \partial y$ represent horizontal and vertical velocities, respectively.

The force balance at the interface (Bernoulli condition) provides the criteria for updating ϕ in time. In the Lagrangian frame of reference required for a coordinate system moving with the interface, the resulting relation becomes [7]

$$\frac{D\phi}{Dt} = -\kappa + \frac{\Gamma_e}{2} q_e^2 + \frac{1}{2} (\nabla \phi \cdot \nabla \phi) \quad (5)$$

where $q_e = \partial \phi_e / \partial n$ represents the electric field strength perpendicular to the local surface. The surface curvature, κ , is evaluated using centered finite differences for a variable spacing mesh to full fourth-order accuracy. This is an important consideration in problems of this nature since capillary forces are substantial and must be resolved accurately.

Eqs. (4) and (5) are integrated in time using a fourth-order Runge–Kutta scheme. Since the nodes will tend to accumulate in regions of high curvature where the surface is greatly distorted, we employ a regridding procedure at the end of each time step. Values of ϕ , x , and y are fitted with cubic splines along the interface and nodes are then redistributed at equal lengths along the surface. This procedure provides a natural “smoothing” of the surface due to the curvature limiting properties of splines. Other authors have found similar benefits from this approach. Using this method, no special filtering schemes are required to avoid “zig-zag” instabilities noted by numerous other authors.

The one complication associated with the integration stems from the nonlinearity in the Bernoulli equation caused by the dependency of ϕ on both ϕ_e (through q_e) and surface shape (through κ). A stable procedure [7,17] has been developed to address this complication:

- Solve Laplace's equation (Eq. (2)) using the current ϕ value to obtain q on the surface.

- Solve Laplace’s equation in the electrostatic domain to obtain q_e values on the surface.
- Decompose q values into velocities in the x and y directions.
- Advance nodal positions and ϕ values on the interface in time via integration of Eqs. (4) and (5) using current x , y , ϕ , q , and q_e values.
- Regrid the surface and provide solutions to Laplace’s equation to obtain q and q_e values for use in the next time step.

The overall scheme requires five Laplace solutions for velocity and electrostatic potentials per time step; four for the Runge–Kutta integration procedure, and one for the regrid. The following sections highlight results obtained from the code for both single-column and multi-jet configurations.

3. Single-column simulations

The model was validated via grid function convergence studies and comparison with linear theory for a single electrified column. Rayleigh [1] was the first to investigate harmonic oscillations of the column using a linear small-perturbation Fourier analysis. He presumed a sinusoidal oscillation of mode number n in a column which was distorted by a small amount from a perfect circle:

$$r_s = 1 + \varepsilon \cos(n\theta) \sin(\omega t), \quad (6)$$

where ε measures the level of distortion ($\varepsilon \ll 1$). While Rayleigh considered an infinite domain in his analysis, we are forced to consider a finite domain for the electrostatic solution due to the fact that the 2-D Green’s function (Eq. (3)) diverges as $\ln|r|$ as $|r| \rightarrow \infty$.

The computational domain for the single-column simulations is shown in Fig. 2; the outer “ground” location is selected at a distance b radii from the center of the column. Here, we have taken advantage of symmetry about the $y = 0$ plane so we need to compute only in the upper half-plane. Repeating Rayleigh’s analysis the kinematic condition (i.e., $\partial\phi/\partial r \approx \partial\eta/\partial t$) and the boundary conditions (i.e., $\phi_e = 1$ at $r = r_s$ and $\phi_e = 0$ at $r = b$) for this finite domain geometry leads to the following linear solutions to Laplace’s equation for ϕ and ϕ_e , respectively:

$$\phi = \frac{\varepsilon}{n} \cos(\omega t) \cos(n\theta) r^n, \quad (7)$$

$$\phi_e = \frac{-1}{\ln(b)} \left[\ln \frac{r}{b} + \left(\frac{b^{2n}}{1 - b^{2n}} \right) \varepsilon \left(\frac{1}{r^n} - \frac{1}{b^{2n} r^n} \right) \cos(n\theta) \sin(\omega t) \right]. \quad (8)$$

These linearized solutions are valid to order ε^2 for the surface shape in Eq. (6). Using Eqs. (7) and (8) in the Bernoulli equation (Eq. (5)), we obtain a solution for the

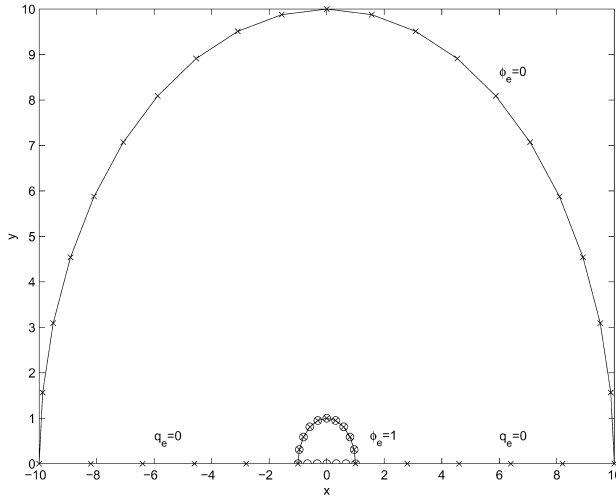


Fig. 2. Schematic of computational domain for a charged liquid column.

harmonic frequencies ($\omega = \omega(n)$) of the column in the finite domain:

$$\omega^2 = n(n^2 - 1) + \frac{n\Gamma_\epsilon}{\ln^2(b)} \left[1 - \left(\frac{1 + b^{-2n}}{1 - b^{-2n}} \right) n \right]. \tag{9}$$

When the ground location is close to the charged cylinder ($b \rightarrow 1$), $\omega^2 \rightarrow -\infty$ in Eq. (9). Therefore, the cylinder is unconditionally unstable in this case.

Fig. 3 shows the neutral stability boundary ($\omega = 0$) as a function of the ground location, b . As the ground is moved outward, larger voltages can be applied and still have stable oscillations. The effect of ground location is investigated for different charging levels. Rayleigh’s original result was written in terms of the charge per unit depth, q'_c on the column. This result can be recovered from Eq. (9) if one lets $b \rightarrow \infty$ and notes that $q'_c \propto V_0'^2/\ln(r')$.

Computations were conducted on the grid in Fig. 2 where the electrostatics nodes are denoted with an “x”, and liquid nodes are labeled with an “o”. We set ϕ_e to 1 and 0 at the interface and the outer-most electrostatic boundaries, respectively. Along the axis $y = 0$ line, we set both q and $q_e = 0$ (on their respective domains) to enforce the symmetry condition. The nonlinear Bernoulli equation (Eq. (5)) provides the boundary condition for ϕ at the interface.

The column is assumed to be initially at rest, but distorted into the shape given by Eq. (6) at the start of calculations. Typical grids employ roughly 150–250 nodes and exhibit computational times from several hours to a couple of days on a Silicon Graphics Indigo 2 machine. Calculations were conducted for various modes, n , and initial distortion levels, ϵ . Grid function convergence studies [12] confirmed that adequate resolution could be obtained using 65 nodes on the interface. For

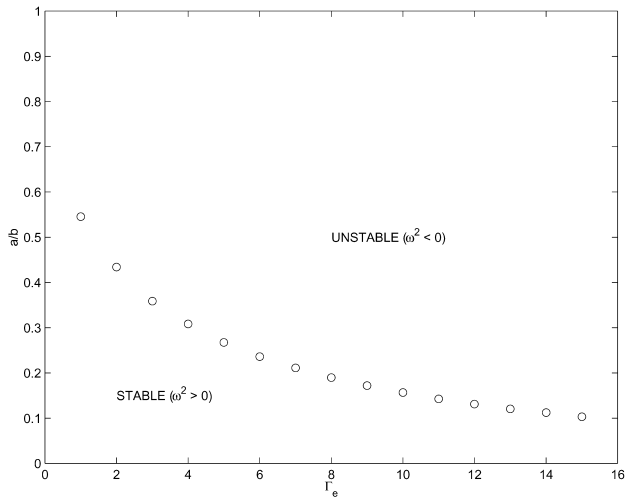


Fig. 3. Stability criteria for the effect of ground location for a column under second-mode deformation.

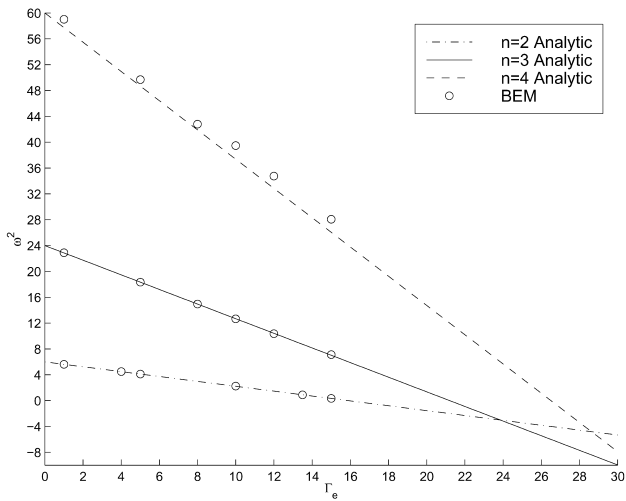


Fig. 4. Comparison of BEM calculations with linear theory for oscillation modes 2–4.

comparison with the linear results (Eq. (9)), a time step of 0.005, $\varepsilon = 0.001$, and $b = 10$, were employed. We computed ω values for modes $n = 2-4$ for various charging levels (Γ_e). Results are compared with Eq. (9) in Fig. 4. Here, $\Gamma_{e,crit}$ is defined as the critical value leading to linear instability of the column ($\omega = 0$ in Eq. (9)).

The results show excellent agreement between calculations and theory, but at high charging levels instabilities were found for both third and fourth modes. The critical

charging level for the second-mode oscillation (from Eq. (9)) is $\Gamma_{e,\text{crit}} \approx 15.9$. While the linear analysis shows that stable oscillations can be obtained in higher modes above this level, our calculations indicate this is not possible. Above $\Gamma_e = 15.9$, all simulations indicate a column instability in second mode regardless of initial shape. Since numerical roundoff errors always will provide some second-mode information for higher mode cases, all columns with Γ_e greater than 15.9 will be unstable. Of course, pure higher-level mode shapes ($n > 2$) will not be found in experiments due to the inherent chaos introduced by tiny fluctuations and geometric imperfections. For this reason, we expect a similar behavior such that instability will result at charging levels above the $n = 2$ critical value for *any* mode shape.

At charging levels exceeding the critical value, the column no longer oscillates, but instead diverges to a highly distorted shape in a monotonic fashion. Highly thinned surfaces appear, and ultimately a “spike” is produced locally due to the dominance of the electrostatic forces in this situation. The shapes formed at this “pinching” event are shown for $\Gamma_e = 2\Gamma_{e,\text{crit}}$ for three different initial second-mode deformation levels (Fig. 5). As the height of the initial perturbation is increased, there is an increased tendency to pinching at two lobes rather than four. From Eq. (9), at the charging level employed, both second and fourth modes are unstable; preference is given to the second mode if the initial deformation level is increased.

The effect of initial distortion level on oscillation frequency is shown for a variety of Γ_e values in Fig. 6. As the initial distortion (ε) increases, we note a decrease in the natural frequency. This phenomenon has been noted with uncharged columns and droplets; it is attributed to the fact that the fluid has farther to move when ε increases. (Recall that the linear analysis presumes essentially no surface movement since it is valid only for vanishingly small ε .) We note that the results are independent of

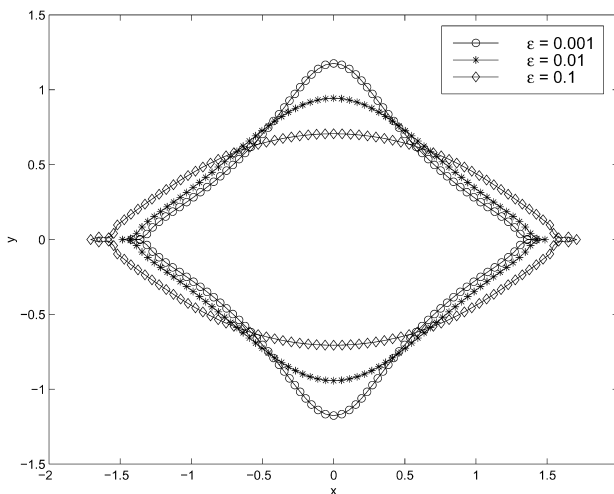


Fig. 5. Pinch geometry for a single column in mode 2 with various initial distortion levels, ε , at $\Gamma_e = 2\Gamma_{e,\text{crit}}$ using 65 nodes on the free surface.

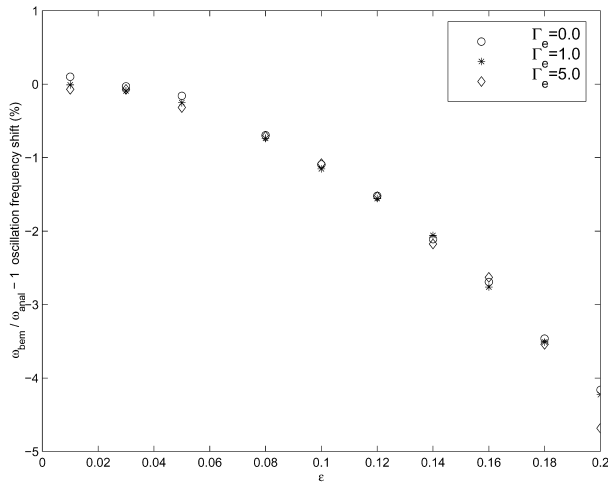


Fig. 6. Nonlinear frequency shift for a jet at various charging levels, Γ_e .

charging level over the range investigated. The reader should keep in mind that these results are restricted to cases where the equipotential jet assumption is valid.

4. Multi-jet simulations

Having validated the model against single-column results, we pursued the multi-jet configuration. Experiments have shown that, under certain conditions, a very stable and repeatable jet structure is obtained for fluids with a limited range of conductivities. The origins and stability of this configuration were explored using the BEM tool described in the previous sections. Initially, we explored the possibility of having a single jet bifurcate azimuthally to form the structure noted in Fig. 1. Linear analysis of a charged column subject to both axial and azimuthal perturbations (as discussed in Refs. [3,4]) revealed that the axisymmetric modes were preferred, i.e. they exhibited the highest growth rate over all unstable wavelengths.

For this reason, linear theory could not support the notion of a single jet bifurcating azimuthally to form the multi-jet structure. In fact, experiments tend to show the multiple ligaments being established on a hemispherical liquid cup which is attached to the exit of the orifice. For these reasons, we chose to pursue stability considerations for a variety of equal sized ligaments spaced at equal intervals about the perimeter of the orifice exit. The idealized geometry, which does not consider three-dimensional (3-D) effects near the liquid cup, is shown in Fig. 7. Electrostatic repulsion between the charged ligaments and capillary forces were theorized to lead to the stable configurations found experimentally. Grid modifications were performed to permit consideration of this geometry. Taking advantage of the symmetry about the centerline of

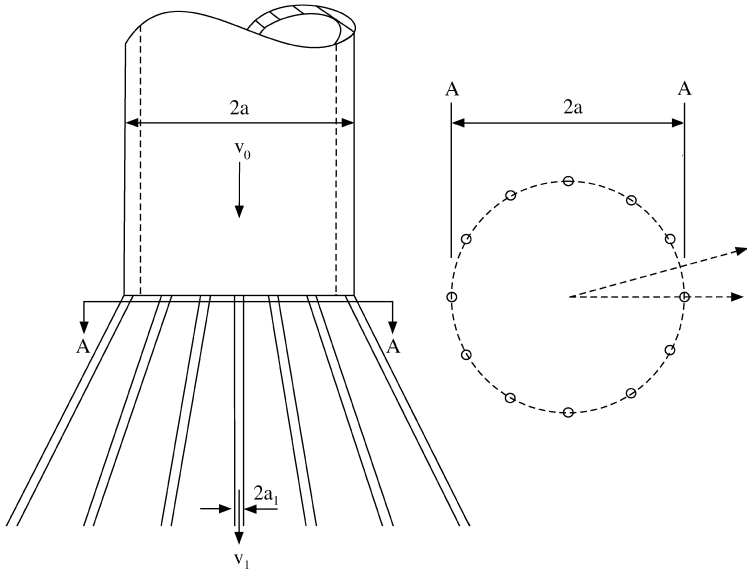


Fig. 7. Schematic of multi-jet atomization.

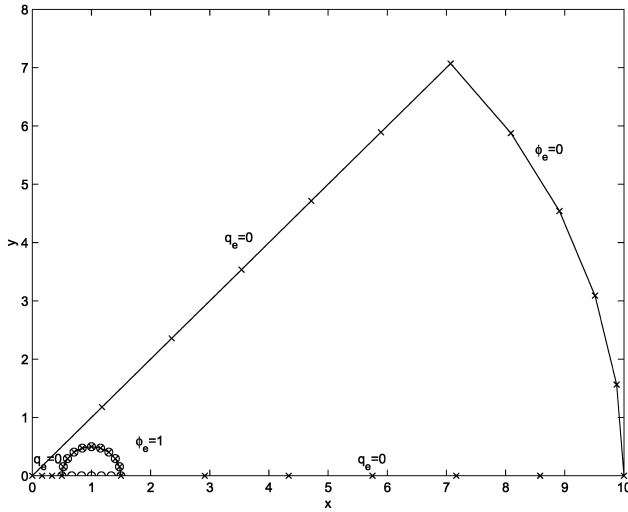


Fig. 8. Schematic of computational domain for multi-jet simulations.

a column and between columns as shown in Fig. 7, we arrive at the sector-shaped computational domain shown in Fig. 8.

The revised code was validated by simulating a single-jet on the multi-jet grid shown in Fig. 8. This simulation was conducted by applying an analytic boundary

condition (Eq. (8)) on all the outer electrostatic boundaries. The frequency of oscillation (for $n = 2$ and $\Gamma_e = 1.0$) was found to agree within 0.1% of the analytic value for this set of conditions.

4.1. Energy analysis: investigation of stable multi-jet configurations

As mentioned previously, one of the goals of the study was to determine the conditions which lead to stable multi-jet operation with a fixed number of ligaments, n_l . Experimentally, it has been shown that increasing voltage leads to an increase in the number of ligaments. We hypothesize that this trend could be explained by a consideration of the relative importance of electrostatic (U_e) and capillary (U_c) surface energies. The electrostatic energy depends on the voltage and the arrangement (geometry) of the columns. The supposition is that when $U_e/U_c \geq 1$ for a given number of columns, we will have sufficient electrostatic energy to fractionate into a larger number of columns. The number of jets can then be predicted by computing the critical charging level, $\Gamma_{e,crit}$, for a given number of ligaments, n_l .

The capillary energy per unit depth is simply the product of the ligament perimeter and surface tension, $U'_c = \sigma 2\pi a'_l$. For a perfect conductor, the electrostatic energy can be written as

$$U'_e = \frac{\epsilon'_0}{2} \left[\int_{V'} \mathbf{E}^2 dV' \right]. \quad (10)$$

Therefore, the ratio of the two energies, in dimensionless form, can be expressed as

$$\frac{U_e}{U_c} = \frac{\Gamma_e}{2\pi a'_l} S_n, \quad (11)$$

where

$$S_n = \left[\int_V \mathbf{E}^2 dV \right]. \quad (12)$$

Unfortunately, volume integrations are challenging when one uses a boundary element solution methodology because we do not have any grid points at internal nodes with which to evaluate the volume integral. We do not generally wish to generate a grid on the interior because the geometry is variable for a time-dependent simulation. Therefore, we utilize a Monte Carlo integration scheme [18] in which random points are picked within the domain and the integral is simply represented:

$$\int_V \mathbf{E}^2 dV \approx \left(\frac{1}{N} \sum_{i=1}^N E_i^2 \right) V, \quad (13)$$

where N is the total number of random points and E_i^2 is the square of the electric field at the point selected:

$$E_i^2 = \left(\frac{\partial \phi_e}{\partial x_i} \right)^2 + \left(\frac{\partial \phi_e}{\partial y_i} \right)^2. \quad (14)$$

We can use the BEM formulation to derive integral representations for $\partial\phi_e/\partial x_i$ and $\partial\phi_e/\partial y_i$ by differentiating Eq. (2). For example, differentiation with respect to x_i gives

$$\frac{\partial\phi_e}{\partial x_i} = \frac{1}{\alpha} \int_S \left[\phi_e \frac{\partial^2 G}{\partial n \partial x_i} - q_e \frac{\partial G}{\partial x_i} \right] dS \tag{15}$$

with an analogous result for the y -direction. The derivatives $\partial^2 G/\partial n \partial x_i$ and $\partial G/\partial x_i$ have been computed analytically for the case of the 2-D Green’s function [19,20]. Performing these integrations using the present methodology permits rapid evaluation of the electric field anywhere in the domain. We can then evaluate E_{x_i} and E_{y_i} using these analytic kernels.

Using this procedure, the electric field is determined at random points and the integral S_n is computed. Roughly 10,000 points were used to get a converged integral. Fig. 9 depicts the electric field strength in the region near the ligament assuming four ligaments with radius equal to the orifice radius. For this very large ligament, strong gradients are present on the back side of the ligament as well as the region between ligaments. In the center of the domain, the field levels are very small.

The ligaments formed in a multi-jet mode tend to be much smaller than the orifice. This case is investigated in Fig. 10 which shows the electric field in the proximity of a small ligament whose diameter is just 3% of that of the flow orifice. This ligament diameter is in the size range observed in the experiments [8,9]. In this case, the field is distorted only slightly from that of a charged wire in an infinite medium. There is a nonnegligible asymmetry created by the presence of neighboring ligaments.

Given the electric field solution, the electrostatic energy can be computed for a given configuration. Since we have nondimensionalized all voltages, the electric field

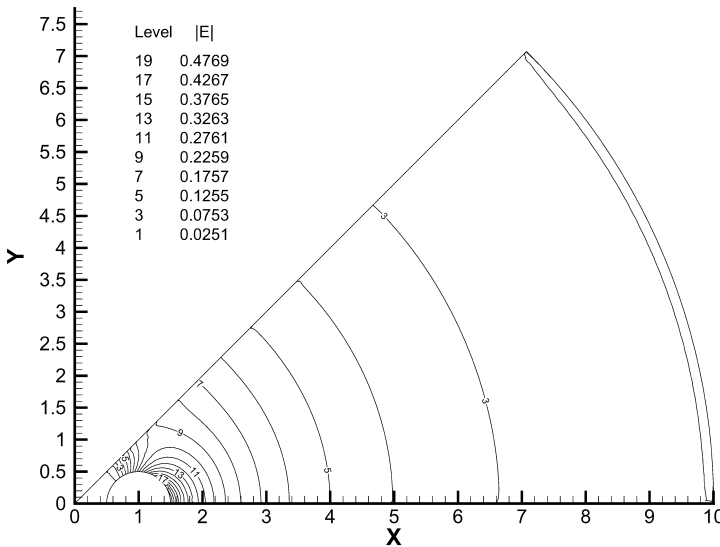


Fig. 9. Electric field distribution near a charged ligament, $a_r = 0.5$ and $n_r = 4$.

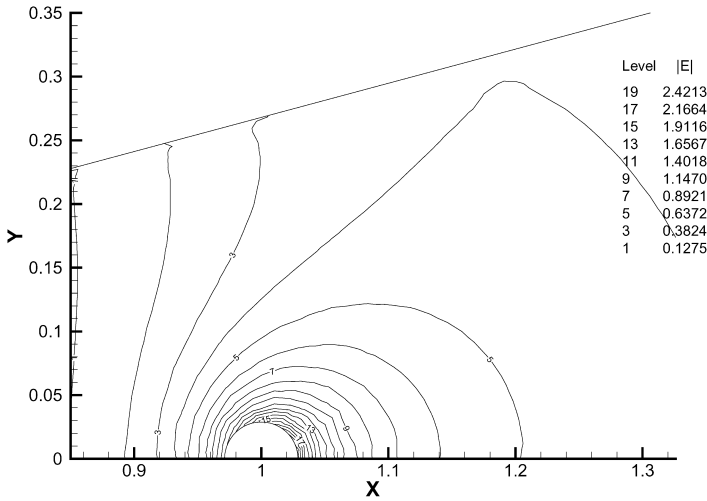


Fig. 10. Electric field distribution near a charged ligament, $a_l = 0.0289$ and $n_l = 12$.

and the integral S_n depend only on the ligament radius, a_l , the number of ligaments, n_l , and the ground location, b . For a given configuration, the integral is evaluated and then the critical charging level, $\Gamma_{e,crit}$ can be determined from Eq. (12) when $U_e/U_c = 1$. Beyond this voltage, we presume that enough electrostatic energy is available to cause subdivision of the ligaments into a new topology.

We can assess the agreement of the model by comparing against experimental data collected during these studies. Table 1 provides a summary of experimental data relevant to this comparison. A more detailed discussion of the experimental apparatus and measurement techniques can be found in Refs. [8,9]. Isopropyl alcohol was doped with varying amounts of ammonium chloride to form fluids with electrical conductivities (k) between 0.04 and 0.4 $\mu\text{S/m}$. Liquid electrical conductivity and dielectric constant were measured using a commercially available insertion meter. Compositions were such that liquid density (790 kg/m^3), viscosity (0.0023 Pa s), and surface tension (0.021 N/m) remained fixed. The orifice diameter was also fixed at 1.55 mm and the flow rate range of the fluid was 60–240 ml/h. Ligament velocities (v_l) were measured using a phase Doppler particle analyzer (PDPA) and ligament diameters (d_l) were computed using the measured velocities and mass flows assuming fluid was evenly distributed amongst all ligaments. Note that very tiny ligaments are produced under these conditions; breakup of these small columns leads to spray Sauter mean diameters (SMD or D_{32}) in the range of 10–40 μm [9].

For each of the data points in Table 1, the energy analysis was applied and the critical voltage level was determined (V_{bem}) assuming $U_e/U_c = 1$. Voltages resulting from this calculation varied from 1 to 3 kV, while the experimental results were about 12–24 kV. Ratios of the two voltages are shown in Fig. 11. These results show a very poor correlation; the actual charge levels required are roughly an order of magnitude larger than those predicted using the simplified energy analysis.

Table 1
Summary of experimental data collected by Epperson and Sojka [11,12]

k ($\mu\text{S/m}$)	Q (ml/h)	V_0 (V)	I (μA)	v_c (m/s)	n_c	d_c (μm)
0.04	60	9.7	4.1	4.1	10	22.8
0.04	60	10.0	2.6	3.8	12	21.6
0.04	60	11.0	2.8	4.0	21	15.9
0.04	60	11.9	3.1	3.4	30	14.4
0.04	120	11.7	4.4	3.7	14	28.6
0.04	120	12.3	4.7	3.5	17	26.7
0.04	120	13.2	5.2	4.0	24	21.0
0.04	120	13.6	5.4	3.5	26	21.6
0.04	120	14.5	5.7	3.9	31	18.7
0.04	180	13.3	6.7	6.1	11	30.8
0.04	180	13.4	5.8	4.5	17	28.9
0.04	180	15.3	8.8	5.9	21	22.7
0.04	180	16.0	9.0	6.1	25	20.4
0.20	60	11.4	5.4	6.5	8	20.2
0.20	60	12.0	6.5	6.1	10	18.7
0.20	60	12.8	7.5	6.4	13	16.0
0.20	60	13.7	8.4	5.7	17	14.8
0.20	60	14.7	9.5	4.3	22	15.0
0.20	120	14.7	12.3	9.5	14	17.9
0.20	120	15.2	13.2	10.1	16	16.2
0.20	120	16.4	14.7	9.4	21	14.7
0.20	120	17.7	16.5	8.8	25	13.9
0.20	120	18.3	17.1	9.7	27	12.7
0.20	180	17.0	15.6	8.2	13	24.4
0.20	180	17.3	16.5	9.4	15	21.2
0.20	180	17.8	17.7	9.9	17	19.4
0.20	180	19.0	19.8	10.5	20	17.4
0.20	180	19.6	21.0	10.0	22	17.0
0.40	60	12.7	8.7	8.8	8	17.4
0.40	60	13.3	10.5	9.2	11	11.0
0.40	60	14.9	11.4	9.4	14	14.0

Since the ground location in the simulations was chosen arbitrarily, we investigated its effects on results and found that this factor could not explain the large voltage discrepancies. The electric field drops rapidly as one moves away from the charged ligaments and there is little electrostatic energy in the domain near the ground.

Another effect warranting consideration is the three dimensionality of the flow field in the region near the ligament formation points. The contributions of the charged hemispherical liquid cup would contribute additional potential to the region between the ligaments. However, in the assumed geometry, this is already a nearly equipotential region as shown in Figs. 9 and 10. Therefore, contributions from the hemispherical cup may not prove to be of great importance. A full 3-D analysis would be required to confirm this supposition.

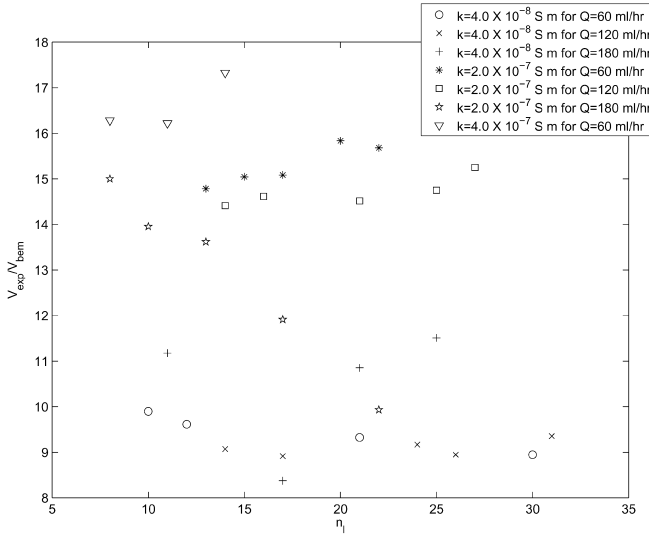


Fig. 11. Comparison of measured (V_{exp}) and computed (V_{bem}) voltages for various numbers of ligaments.

To further investigate discrepancies between the model and the experimental results, the voltage drop down a ligament of length ℓ was estimated as

$$\Delta V = I_{\ell} \frac{l}{k\pi a_{\ell}^2}, \quad (16)$$

where I_{ℓ} is the current in the ligament and k is the fluid electrical conductivity. Experimental images indicate the ligament intact length to be of the order of 1 mm. If one assumes the measured current is equally divided among the n_{ℓ} ligaments with no current leakage outside the system, ligament voltage drops of the order of 10^8 V are estimated from the data in Table 1. Even if only a small fraction of the supplied current enters each ligament, the voltage drop easily exceeds the applied voltage due to the very high effective resistance of these 10–30 μm diameter cylinders. Data from cone jet studies [14] indicate that conduction (ohmic) currents dominate the cone region while convection currents dominate in the jet. We expect a similar behavior in this case; this factor also aids in explaining the discrepancies between model and experiment.

For this reason, the equipotential, perfect conductor assumption applied in the analysis is poor and can be regarded as accurate only over very small lengths of the ligament. Presuming that the analysis can be applied just at the entry to the ligament, and that the voltage levels predicted by the analysis are correct, we can compute the effective resistance for entering a given ligament as

$$R_{\text{eff}} = V_{\text{bem}} n_{\ell} / I, \quad (17)$$

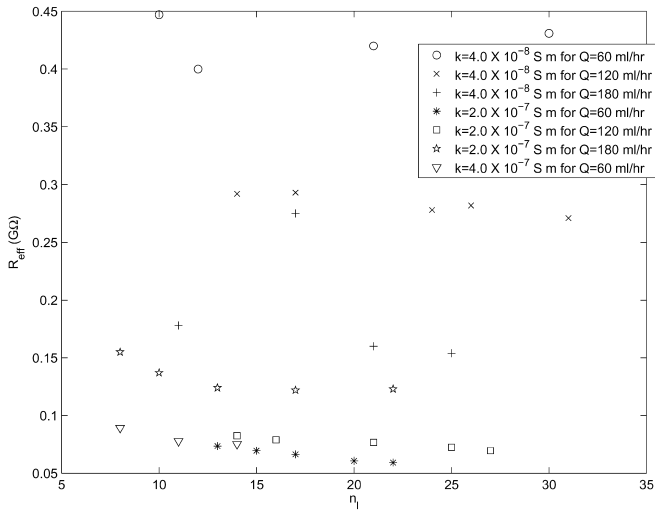


Fig. 12. Effective resistance (R_{eff}) in the ligament vs. n_l .

where I is the measured current. Here, we assume there is no current leakage and that the applied current is equally divided among the ligaments.

Fig. 12 provides a comparison of R_{eff} values for the data in Table 1 utilizing the critical voltages predicted from the BEM model. For all cases investigated, the effective resistance is very large and appears to be insensitive to the number of ligaments formed. For the higher conductivity cases, R_{eff} is also insensitive to flow rate. Even for the low-conductivity case, this effective resistance only varies by about $\pm 50\%$ for a three-fold change in flow rate. For this reason, the energy analysis can conceivably be applied by using Eq. (17) to compute the necessary V_{bem} for a known R_{eff} and current. An iterative approach would be required because one would have to presuppose the number of ligaments before the voltage could be computed and the voltage itself depends on the number of ligaments. The real drawbacks to this approach are that the current must be known a priori and that current leakage is neglected; at best the technique could be applied for a fixed experimental configuration. Nevertheless, such an approach could be utilized as a predictive tool to determine a priori the jet configuration should the current value be measured or estimated.

5. Conclusions

Nonlinear simulations have been conducted for single- and multiple-charged liquid columns using a boundary element technique under the assumption of equipotential liquid surfaces. The single-column results show that the column is unstable in

all modes if the primary charging limit for the $n = 2$ mode is exceeded. For small deformations, column oscillations agree well with linear theory. For larger deformations, oscillations frequencies are reduced due to the fact the fluid has a finite distance to travel in these cases. This nonlinear frequency shift has been shown to be independent of charging level. Simulations were conducted for unstable columns showing pinching into “spiked” shapes with primarily second-mode behavior.

The multi-column geometry was also investigated. This geometry takes into account the experimentally observed symmetry associated with the multi-jet electrostatic atomization mode. An energy analysis was conducted to determine conditions when electrostatic energy exceeded capillary energy. The critical voltage determined from this condition is far below the experimental operating voltages required to sustain the multi-jet mode; voltage drops within the ligaments are shown to be very large comparable to the charging potential. Through the use of an effective resistance entering the ligament, or analogously an effective current in the ligament, the energy analysis can remove the sensitivity of these parameters to the number of ligaments and does represent the first step toward a fully predictive capability.

References

- [1] L. Rayleigh, On the equilibrium of liquid conducting masses charged with electricity, *Philos. Mag.* 14 (1882) 184–186.
- [2] L. Rayleigh, On the instability of jets, *Proc. London Math. Soc.* 10 (1878) 4–13.
- [3] J.R. Melcher, *Field-Coupled Surface Waves*, MIT Press, Cambridge, MA, 1963.
- [4] J.M. Schneider, N.R. Lindblad, C.D. Hendricks Jr., J.M. Crowley, Stability of an electrified liquid jet, *J. Appl. Phys.* 38 (1967) 2599–2605.
- [5] A.B. Basset, Waves and jets in a viscous liquid, *Am. J. Math.* 16 (1894) 93.
- [6] R.J. Turnbull, Self-acceleration of a charged jet, *IEEE Trans. Ind. Appl.* 25 (1989) 699–704.
- [7] E.R. Setiawan, S.D. Heister, Nonlinear modeling of an infinite electrified jet, *J. Electrostat.* 42 (1997) 243–257.
- [8] J.T. Epperson, P.E. Sojka, Formation of near-monodisperse sprays using an electrostatic atomizer operating in multi-jet mode, *ILASS Americas-98 Proceedings*, 1998, pp. 214–218.
- [9] J.T. Epperson, P.E. Sojka, Ligament formation for an electrostatic atomizer operating in multi-jet mode, *ILASS Americas-99 Proceedings*, 1999, pp. 231–235.
- [10] E. Cohen, C.J. Somol, D.A. Gordon, A 100-kV, 10-W heavy particle thruster, Paper AIAA 65-377, AIAA second Annual Meeting, San Francisco, CA, 1965.
- [11] M. Cloupeau, B. Prunet-Foch, Electrostatic spraying of liquids: main functioning modes, *J. Electrostat.* 25 (1990) 165–184.
- [12] J. Fernandez de la Mora, The effect of charge emission from electrified liquid cones, *J. Fluid Mech.* 243 (1992) 564–574.
- [13] L. Cherney, Structure of Taylor cone-jets limit of low flow rates, *J. Fluid Mech.* 378 (1999) 167–196.
- [14] A.M. Ganan-Calvo, Cone-jet analytical extension of Taylor’s electrostatic solution and the asymptotic universal scaling laws in electrospraying, *Phys. Rev. Lett.* 79 (1997) 217–220.
- [15] S.D. Heister, M. Rutz, J. Hilbing, Effect of acoustic perturbations on liquid jet atomization, *J. Propulsion Power* 13 (1) (1997) 82–88.
- [16] C.A. Spangler, J.H. Hilbing, S.D. Heister, Nonlinear modeling of jet atomization in the wind-induced regime, *Phys. Fluids* 7 (5) (1995) 964–971.
- [17] S.D. Heister, Boundary element methods for two-fluid free surface flows, *Eng. Anal. Boundary Elements* 19 (4) (1997) 309–317.

- [18] G.S. Gipson, *Boundary Element Fundamentals*, Vol. 2, Computational Mechanics Publications, Southampton, 1987.
- [19] S.S. Yoon, *Simulation of the nonlinear dynamics of charges liquids using boundary elements*, M.S. Thesis, Purdue University, 1999.
- [20] S.S. Yoon, S.D. Heister, Analytic solution for fluxes at interior points for the 2-D Laplace equation, *Eng. Anal. Boundary Elements* 24 (2) (2000) 155–160.